Hypoxia-responsive luminescent CEST MRI agent for *in vitro* and *in vivo* tumor detection and imaging

Sanu Karan[1,2,†], Mi Young Cho[1,†], Hyunseung Lee[1], Hye Sun Park[1], Eun Hee Han[1], Youngkyu Song[3], Youlee Lee[3], Mina Kim[4], Jee-Hyun Cho[3,*], Jonathan L. Sessler[5,*], Kwan Soo Hong[1,2,*]

[1]Research Center for Bioconvergence Analysis, Korea Basic Science Institute, Cheongju 28119, Korea

[2]Graduate School of Analytical Science and Technology, Chungnam National University, Daejeon 34134, Korea

[3]Research Equipment Operations Division, Korea Basic Science Institute, Cheongju 28119, 34134, Korea

[4]Department of Neuroinflammation, UCL Queen Square Institute of Neurology, Faculty of Brain Science, London WC1N 3BG, United Kingdom

[5]Department of Chemistry, The University of Texas at Austin, Austin, Texas 78712-1224, USA

KEYWORDS: Chemi-luminescent; CEST imaging; Hypoxia; Cancer cell imaging

ABSTRACT: Hypoxia is a feature of most solid tumors and a key determinant of cancer growth and propagation. Sensing hypoxia effectively could lead to more favorable clinical outcomes. Here, we report a molecular antenna-based bimodal probe designed to exploit the complementary advantages of magnetic resonance (MR)- and optical-based imaging. Specifically, we describe the synthesis and evaluation of a dual action probe (**NO_2-Eu**) that permits hypoxia-activated chemical exchange saturation transfer (CEST) MR and optical imaging. In CT26 cells, this **NO_2-Eu** probe not only provides an enhanced CEST MRI signal, but also turns "ON" the optical signal under hypoxic conditions. Time-dependent in vivo CEST imaging in a hypoxic CT26 tumor xenograft mouse model revealed probe-dependent tumor detection by CEST MRI contrast in the tumor area. We thus suggest that dual action hypoxia probes, such as the one reported here, could have a role to play in solid tumor diagnosis and monitoring.

■ INTRODUCTION

Hypoxia is a hallmark of solid tumors and can lead to an upregulation of hypoxia-inducible factors, such as HIF-1α and HIF-β.[1] It also affects key biological processes, including cell proliferation, angiogenesis, pH regulation, apoptosis, immortality, and migration.[2–4] Chronic hypoxia results from outgrowing the blood supply due to uncontrolled cell proliferation in tumors, while at the cellular level, hypoxia is caused by reduced oxygen diffusion rates with increasing distance from the vasculature; this can result in 'delivery hypoxia',[5] as well as 'consumptive hypoxia' wherein the cancer cells consume oxygen faster than the oxygen delivered.[6] Moreover, hypoxia can spread heterogeneously within solid tumors and can lead to such tumors becoming metastatic in nature.[7] Importantly, the low oxygen tension ($pO_2 \leq 20$ mm Hg) characteristic of hypoxia can influence the efficacy of current

anticancer treatments.[8] For example, the low oxygen levels associated with hypoxia can render tumors resistant to radiation due to the insufficient formation of reactive oxygen species that result in lethal damage to the tumor DNA.[9] Additionally, hypoxia-driven HIF-1α/β upregulation and the presence of free radical species induces angiogenesis that can reduce the effectiveness of radiation therapy.[10] The efficacy of chemotherapeutics can also be reduced by tumor hypoxia. For instance, chemotherapeutics may experience obstacles in reaching the hypoxic region of head and neck cancer when administered through the bloodstream.[11] Moreover, the acidic extracellular environments typically associated with hypoxic conditions can restrict the extracellular uptake of chemotherapeutics.[12] Being able to map hypoxia and understanding the underlying determinants could lead to improvements in disease control, including cancer management. Here we describe the synthesis and evaluation of a dual action probe that permits hypoxia-activated chemical exchange saturation transfer (CEST) magnetic resonance (MR) and optical imaging of hypoxic tissues. It exploits the complementary strengths of these disparate modalities allowing for potential enhancements in diagnostic capability.

To date several methods have been employed for mapping hypoxic tumors.[13–15] Among these, fluorescent probes have received particular attention because they can provide high spatiotemporal images in living cells. Although optical hypoxia sensors are relatively sensitive, due to light propagation issues, they show limited applicability for monitoring hypoxia levels *in vivo*.[16,17] Thus, optical-based hypoxia sensors are largely restricted to tissue-based imaging. In contrast, magnetic resonance imaging (MRI) has become established as a preeminent *in vivo* diagnostic technique because tissue penetration is not a limiting factor.

We report here an emissive probe (**NO_2-Eu**) for tumor hypoxia detection and cancer cell imaging. This hypoxia-activatable luminescence probe incorporates DOTA bearing a 3-nitropthalimide group as an NADPH-nitroreductase (NTR)-sensing moiety. A considerable body of prior work on optical-based hypoxia sensors,[18-21] provides support for the design expectation that the 3-nitropthalimide moiety present in the **NO_2-Eu** probe will be reduced to a primary aromatic amino group by NTR in

the presence of nicotinamide adenine dinucleotide (NADH). Intramolecular charge transfer (ICT) from the resulting free NH_2 moiety to the Eu^{3+} ion would result in a "turn on" in the luminescent signal. In addition, the two protons on the NH_2 group would be expected to exchange with the bulk water, resulting in a "switching on" of a CEST signal allowing hypoxic environments characterized by high NTR levels to be imaged by two separate modalities, namely luminescence and CEST MRI. As detailed below, this approach has been validated at the cellular level via optical imaging of live *Escherichia coli* (*E. coli*) cells, as well as *in vitro* CEST MRI studies involving CT26 cancer cells. Moreover, using the present NO_2-Eu probe, hypoxic tumors could be detected *in vivo* in a CT26 xenograft mouse model.

A number of reducing enzymes (e.g., NADPH-NTR, NADPH-cytochrome P450 reductase, cytochrome b5 reductase, xanthine oxidase, and DT-diaphorase) are correlated with hypoxia in mammalian cells.[17] As a result, readily reducible moieties, such as nitroaromatic compounds, azo-derivatives, and quinones, have been explored in the context of creating hypoxia-sensitive markers.[22–25] Optical probes capable of detecting NTR activity in bacterial lysates have also been reported.[26-28] Unfortunately, the majority of the systems investigated to date have failed to provide clear images *in vivo*, presumably due to the short lifetime of the fluorescence signal and self-quenching of the near infrared dye.[16]

MRI provides an attractive complement to optical-based imaging due to its high spatial resolution, essentially unlimited penetration depth, and lack of harmful radiation.[29–31] The unique MR frequencies of CEST agents provide the ability to specifically detect the agents and their respective biomarkers, relative to conventional MRI. Current CEST agents work by selectively reducing the magnetization of the water signal with minimal effects on its longitudinal relaxation rate. In practice, this requires molecules that contain exchangeable protons and use of the magnetization transfer nuclear magnetic resonance (MT-NMR) technique introduced by Forsen and Hoffman in 1963.[32]

In 2012, Sherry and coworkers introduced paramagnetic chemical exchange saturation transfer (para-CEST)-based europium(III) DOTA-tetra amide complexes that function as redox-active MRI sensors (DOTA = 1,4,7,10-tetraazacyclododecane-1,4,7,10-tetraacetic acid).[33] In addition, para-CEST MRI contrast agents have been used to detect caspase-3, an important apoptosis biomarker.[34] pH-responsive para-CEST agents have also been reported for detecting changes in the kidney pH levels.[35] Other pH-sensitive[36–38] as well as Zn(II)-responsive CEST MRI probes are known.[39] However, to the best of our knowledge, hypoxia-responsive CEST probes have yet to be described. The goal of the present study was thus to prepare such a probe, namely **NO_2-Eu**, and test whether it would allow for the combined MR- and optical-based imaging of hypoxic cells and tissues.

■ RESULTS AND DISCUSSION

Design and synthesis of the NO_2-Eu

Probe **NO_2-Eu** was prepared as follows: Initially, 2-(2-hydroxyethyl)-4-nitroisoindoline-1,3-dione (compound **2**) was synthesized by condensing 3-nitrophthalic anhydride (Compound **1**) with ethanolamine in ethanol under reflux conditions (Scheme S1). Compound **3**, namely 2-(2-bromoethyl)-4-nitroisoindoline-1,3-dione, was then obtained through the bromination of **2** using *N*-bromosuccinimide (NBS) and triphenylphosphine in DMF at 85°C. Following the selective protection of 1,4,7,10-tetraazacyclododecane (CYCLEN) by triple *N*-alkylation with *tert*-butyl bromoacetate,[34] compound **4** (see Scheme S1) was prepared by reacting **3** with **4**, and subsequent deprotection of the *tert*-butyl groups using trifluoroacetic acid. Probe NO_2-Eu in the form of an Eu^{3+}-chelated complex was then obtained by metalating compound **4** with an excess of $EuCl_3 \cdot 6H_2O$. Compounds **2**–**4** and the probe (**NO_2-Eu**) were characterized by ^1H and ^{13}C NMR spectroscopy, and by HR-MS (Figures S1–

S10). The purity of probe **NO_2-Eu** was confirmed by HPLC analysis (Figure S11). **NO_2-Eu** purity is 95.2%.

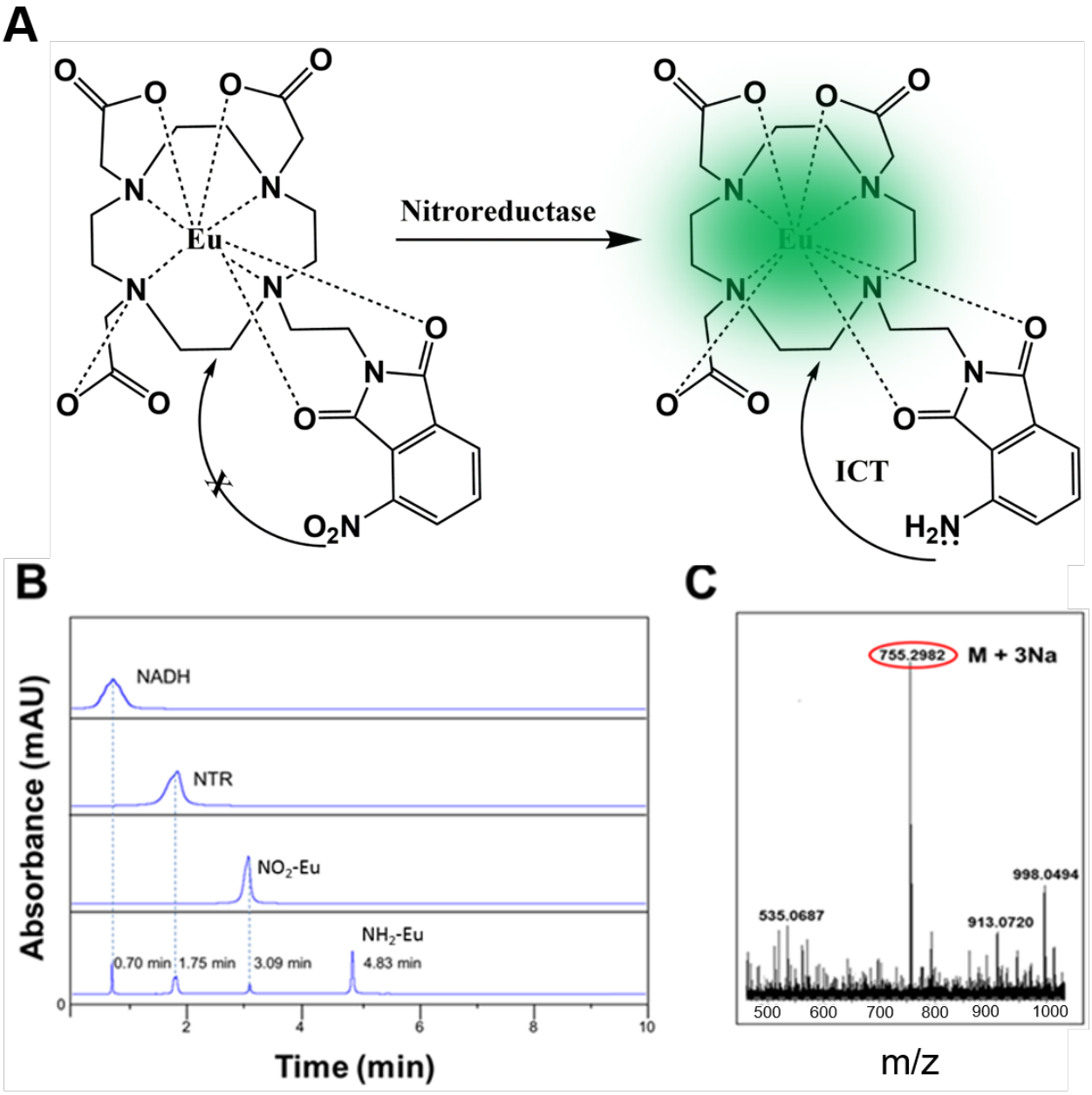

Scheme 1. (A) Schematic representation of the active "switching on" of fluorescence emission intensity as the result of an intramolecular charge transfer (ICT) process resulting from reduction of the nitro moiety in **NO_2-Eu** to the corresponding amine (aniline) form (**NH_2-Eu**) promoted by nitroreductase (NTR). (B) HPLC profile of the **NO_2-Eu** probe (10 μM) in the presence of NTR (1 μg/mL). (C) HRMS data recorded after incubation of probe **NO_2-Eu** (5 μM) with NTR (0.5 μg/mL) for 1 h.

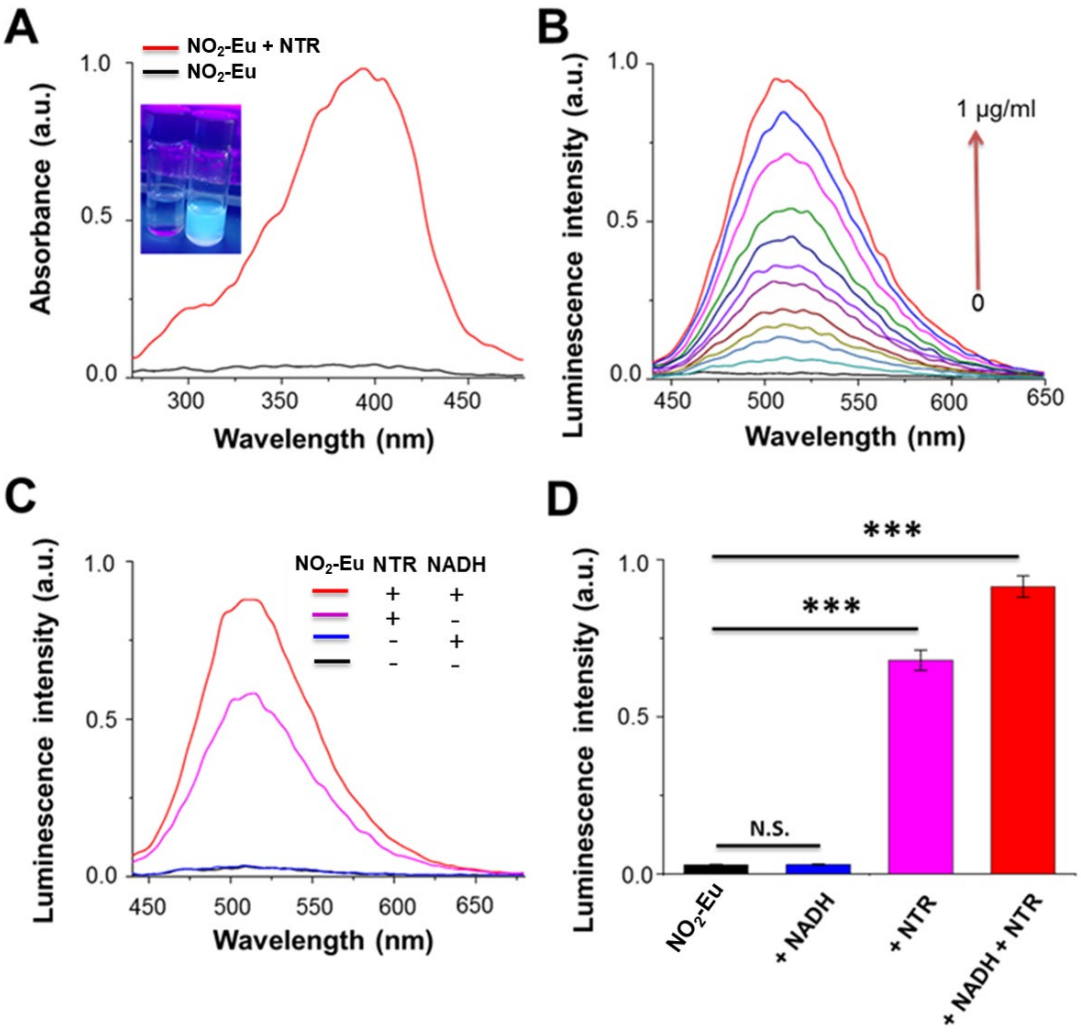

Figure 1. Photophysical properties of probe NO_2-Eu before and after treatment with nitroreductase (NTR). (A) UV absorption spectra of probe **NO_2-Eu** (5 μM) recorded in the presence and absence of NTR. (B) Fluorescence emission (λ_{ex} = 405 nm) spectra of probe **NO_2-Eu** recorded in the presence of various concentrations of NTR (0–1 μg/mL) and nicotinamide adenine dinucleotide (NADH). (C and D) Co-enzyme activity monitored by recording the emission spectrum of probe **NO_2-Eu** in the presence of both NTR and NADH. All experiments were carried out in phosphate-buffered saline (PBS), and the concentrations of the probe and NADH were 5 and 200 μM, respectively. The data shown are averages of four independent experiments; the error bars represent the standard deviations. The *P* values were determined using a nonpaired Student's t-test for homogenous variance. ***<0.001.

Optical properties of the NO_2-Eu

To determine whether NTR could reduce the aromatic nitro moiety in probe **NO_2-Eu** to its corresponding amine (aniline) form, changes in the UV–vis absorption spectra and the luminescence emission of the complex were monitored in the presence of various concentrations of NTR under simulated physiological conditions after first recording the UV absorbance spectrum of **NO_2-Eu** (Figure S12). As shown in Figure 1A, the UV–vis absorption maximum of probe **NO_2-Eu** (5 μM) at 405 nm increased in intensity by ca. 28-fold upon the addition of 1 μg/mL NTR. Likewise, the intensity of the emission feature at 512 nm increased 70-fold when exposed to the same concentration of NTR (Figure 1B).

An HPLC analysis of probe **NO_2-Eu** (10 μM) in the presence of NTR revealed a new band, consistent with the NTR-promoted reduction of the nitro group to an amine (Figure S13). We then monitored the changes in the luminescence intensity of the probe at 512 nm in the presence of both NADH and NTR; it was found that the luminescence intensity reached a maximum at NTR and NADH concentrations of 1 μg/mL and 200 μM, respectively. These spectral changes are attributed to conversion of the nitro (-NO_2) group into the corresponding aniline (-NH_2) group. Intramolecular charge transfer between the lone pair electrons on the NH_2 nitrogen atom and the electron-deficient europium ion is thus switched on, activating the emissive features of probe **NO_2-Eu** (Scheme 1A).

To confirm the NTR-mediated activation of probe **NO_2-Eu**, the probe was treated with 1 μg/mL NTR at 37°C for 30 min. HRMS analysis revealed one major peak reflecting the generation of an activated probe ([M + 3Na] = 755.298) (Scheme 1C).

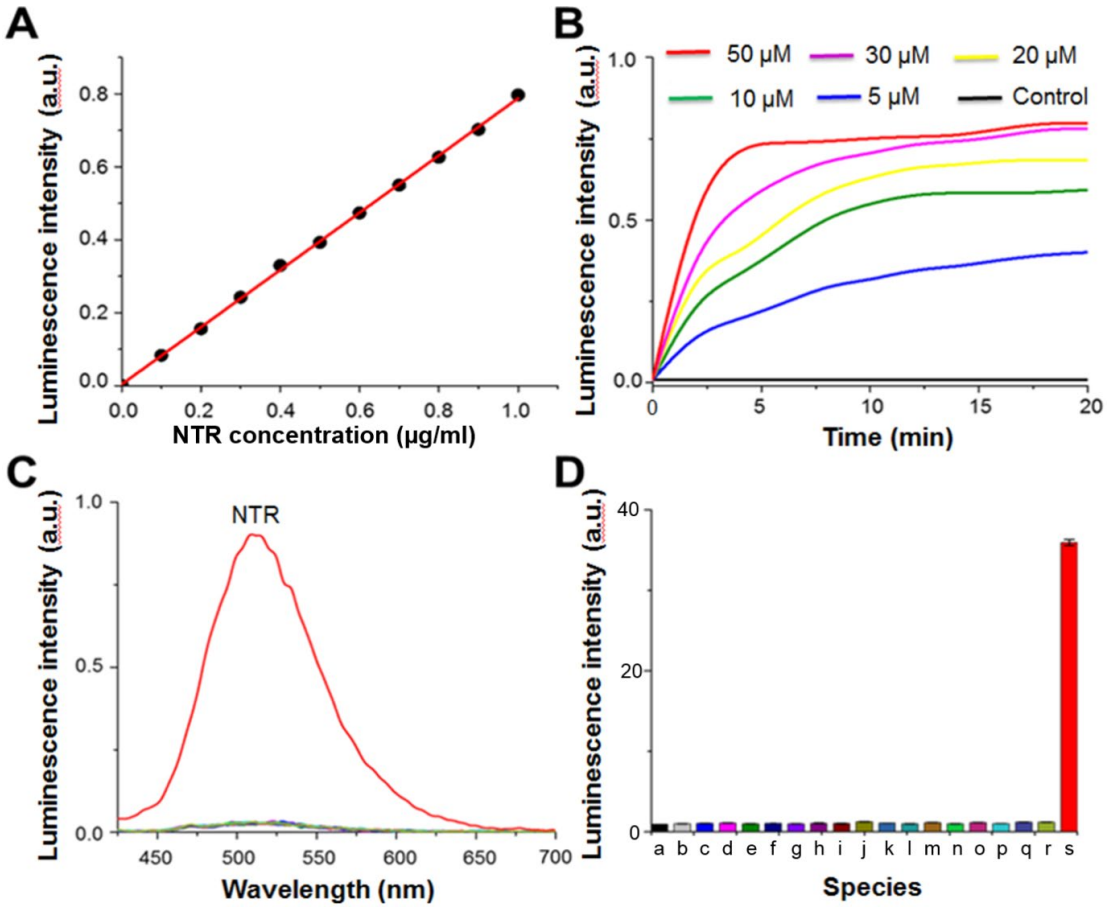

Figure 2. Photophysical properties of probe NO_2-Eu monitored under various experimental conditions. (A) Emission intensity of probe **NO_2-Eu** (5 μM) recorded at various NTR concentrations (pre-incubated for 20 min at 37°C) (λ_{ex} = 405 nm and λ_{em} = 525 nm for all experiments unless noted otherwise). (B) Time-dependent changes in the emission intensity of probe **NO_2-Eu** (5, 10, 20, 30, and 50 μM) observed in the presence of NTR (0.5 μg/mL). (C) Luminescence response of probe **NO_2-Eu** (5 μM) observed in the presence of different potential interferants in blood serum: (a) Blank (probe + NADH in PBS), and containing (b) 150 mM KCl, (c) 2.5 mM $CaCl_2$, (d) 2.5 mM $MgCl_2$, (e) 10 mM glucose, (f) 1 mM vitamin C, (g) 1 mM vitamin B_6, (h) 100 μM HSA, (i) 10 μM H_2O_2, (j) 10 μM $^{\cdot}OH$, (k) 1 mM glutamic acid, (l) 1 mM arginine, (m) 1 mM serine, (n) 5 mM glutathione, (o) 1 mM cysteine, (p) 1 mM homocysteine, (q) 1 mM dithiothreitol, (r) 1 mM lysine, and (s) 1 μg/mL NTR. (D) Quantitative values of the emission intensity at λ_{em} = 525 nm for the same samples depicted in panel (C). Data shown are averages of three independent measurements. All experiments were carried out in the presence of NADH (200 μM).

The luminescence intensity of the **NO_2-Eu** was then monitored as a function of the NTR concentration and time (Figures 2A and 2B) at λ_{em} = 512 nm. The time needed to reach saturated luminescence intensity was gradually shortened with increasing NTR concentration. An increased enzyme concentration accelerates reduction from **NO_2-Eu** to **NH_2-Eu**. Saturation was reached in most cases within ~20 min. The detection limit was determined to be 1.78 ng/mL. Prior to application of probe **NO_2-Eu** to an *in vitro* cellular test system, we examined whether interference was observed in the presence of other biologically relevant analytes. More specifically, the optical properties of the probes were monitored in the presence of non-thiol amino acids (cystine, alanine, histidine, arginine, and tyrosine), biologically relevant metal ions (Na^+, K^+, Ca^{2+}, Fe^{2+}, Fe^{3+}, Cu^{2+}, Mg^{2+}, and Zn^{2+}), and redox active species (ascorbic acid, NO^-, NO_3^-, NO_2^-, H_2O_2, and $S_2O_3^{2-}$). No significant spectroscopic changes were observed in the presence of these potentially interfering analytes (Figures 2C and 2D). Our studies are focused on stability. The issue of specificity for NTR vs. other enzymes remains a subject for future study.

Since blood serum contains significant amounts of NADH and reduced species that might serve to activate the nitro functionality present in probe **NO_2-Eu** prematurely, the stability of the probe was also evaluated in blood serum. No changes in the luminescence intensity were observed, as can be seen in Figure S14, leading us to infer that the **NO_2-Eu** would likely to be stable under most anticipated conditions of use.

In vitro activation of probe NO_2-Eu and imaging of hypoxic CT26 cells

As an initial test of biocompatibility, we assessed the effect of the probe on the CT26 cell line (murine colorectal carcinoma cells) under hypoxic (1% O_2) and normoxic (20% O_2) conditions (Figures S15A and S16). After incubation of the cells with probe **NO_2-Eu** (0–1 mM for 3 h, and 0-20

mM for 24 h), the cell viability was >90%, leading us to infer that this new probe was not appreciably cytotoxic under conditions designed to mimic its use in imaging applications.

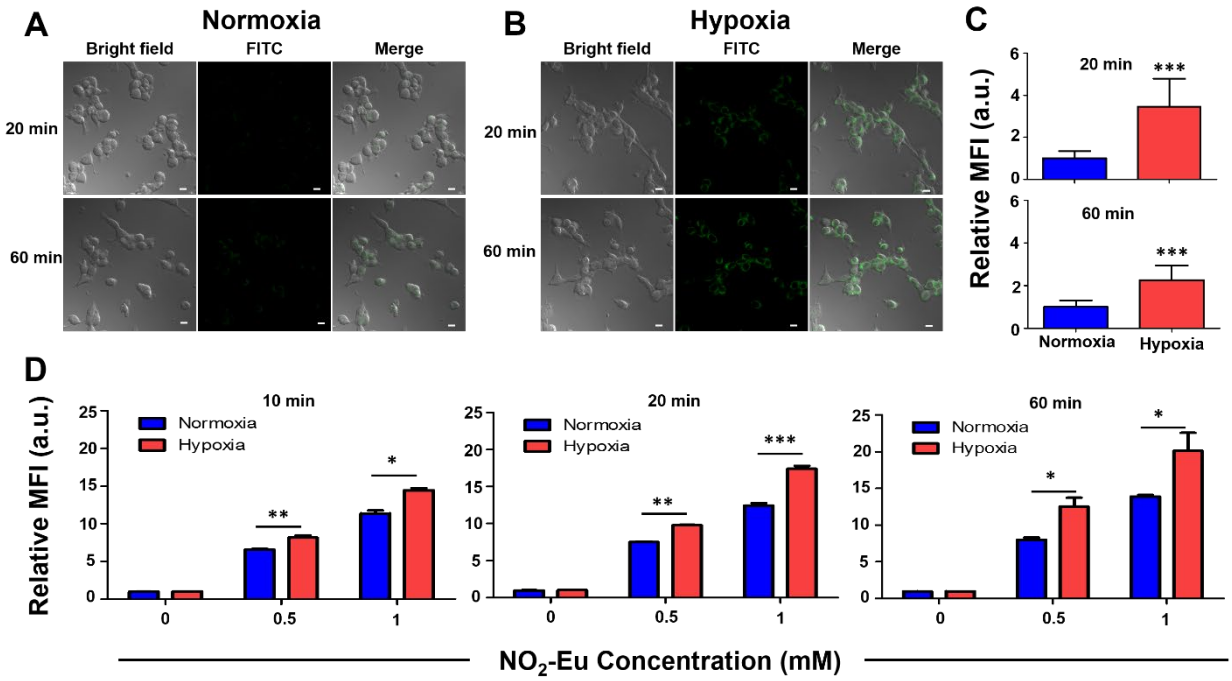

Figure 3. ***In vitro*** **luminescence imaging of CT26 cells**. Representative confocal laser scanning microscopy (CLSM) images of CT26 cells incubated with **NO_2-Eu** (0.5 mM) for 20 min or 60 min under normoxic (A) and hypoxic (1% O_2) (B) conditions, and corresponding quantitative comparison (C) of fluorescent intensities measured from ten individual cells using the ImageJ software (non-paired Student's t-test). Images were obtained using the FITC spectral window. Scale bar, 10 μm. (D) FACS analyses of CT26 cells treated with **NO_2-Eu** (0.5 mM or 1 mM) for 10, 20, or 60 min. The data are averages of three independent experiments; errors bars show the standard deviations (nonpaired Student's t-test). *p < 0.05, **p < 0.01, and ***p < 0.001.

To assess the applicability of the probe in the context of intracellular NTR monitoring, fluorescence-activated cell sorting (FACS) analyses were carried out on CT26 cells under both hypoxic and normoxic conditions for 24 h prior to treatment with probe **NO_2-Eu** (0.5 or 1 mM for 3 h). As shown in Figure S15B, probe **NO_2-Eu** produced a significantly higher luminescent signal in CT26 cells under

hypoxic conditions, a finding that we take as evidence that these cells express NTR under low oxygen tensions. To obtain further insights into the cellular uptake and hypoxia-induced activation of **NO_2-Eu**, we carried out luminescence imaging experiments in CT26 cancer cells treated with **NO_2-Eu** (1 mM) under hypoxic (1%) and normoxic (20%) conditions. Per our design expectations, a more intense luminescence signal was seen under hypoxic conditions (Figure S17). We further investigated the actual time of **NO_2-Eu** activation by using time dependent confocal laser scanning microscopy (CLSM) for live cell imaging. Here, CT26 cells were incubated with **NO_2-Eu** (0.5 mM) under both normoxic and hypoxic (1% O_2) conditions for 20 min or 60 min. As shown Figure 3A and 3B, a strong fluorescent was seen in CT26 cells under hypoxic conditions with the effect being greater than under normoxic conditions. The mean fluorescent intensity (MFI) under conditions of normoxia or hypoxia was determined using the ImageJ software (Java, Maryland, USA) and CT26 cells treated with **NO_2-Eu** (0.5 mM) for either 20 min or 60 min (Figure 3C). These finding revealed that **NO_2-Eu** gives rise to a relatively high MFI under hypoxic conditions. We further confirmed this inference using time dependent FACS analysis; again, the same phenomenon was observed (Figure 3D).

To provide more definitive evidence that hypoxia induces **NO_2-Eu** activation, FACS analyses of **NO_2-Eu** in the presence of the hypoxia inducer of glutathione ethyl ester were performed,[40-42] resulting in higher luminescence intensity compared to the non-treated group (Figure S18). These results taken in concert are considered as evidence that, to the limit of our detection ability, **NO_2-Eu** appears to be activated under hypoxic as well as normoxic conditions, which limits its hypoxia-specific detection utility.

To examine HIF-1α protein expressions in hypoxic or normoxic CT26 cells, we performed Western blot analyses, which revealed that hypoxic CT26 cells have a higher level of HIF-1α protein expression relative to normoxic cells (Figure S19).

In a separate experiment *E. coli* cultures were incubated with probe **NO_2-Eu** and the emission intensity recorded in an effort to assess whether it could be used to assess microbial NTR activity *in vitro*. Here, bacterial cultures were grown and then treated with the probe (0.5 or 1 mM) prior to lysis. As shown in Figure S20, the luminescence intensity was increased by up to 2-fold in the presence of probe **NO_2-Eu**. This provides support for the notion that this new probe may be used to monitor microbial NTR activity.

CEST MRI analysis of the activated NO_2-Eu in solution

We then considered whether activation of probe **NO_2-Eu** could be detected by CEST MRI. Since the reduced probe possesses an aniline NH_2 group that is capable of proton exchange with the surrounding water, saturation of these protons with radio frequency (RF) pulses was expected to result in a decrease in the CEST MRI signal of water (cf. Figure 4A). CEST imaging was then performed to evaluate whether probe **NO_2-Eu** could be used to monitor NTR activity via MRI. With this goal in mind, we performed CEST imaging on phantoms containing either the oxidized or reduced forms of the probe. The latter forms were produced by adding 1 equivalent of NTR. In the CEST spectra and MTR_{asym} (%) plots, only the phantom containing NTR showed a highly enhanced CEST effect (giving a maximum at ~4 ppm), a finding in line with the expected proton exchange between the Eu^{3+}-complexed NH_2-bearing ligand and the bulk water protons (Figures 4B and 4C). A CEST color map showing a significant enhancement for only the phantom containing the added NTR was also constructed (Figure 4D). In this solution phase CEST experiment, a relatively high concentration of **NO_2-Eu** (20 mM), along with a similar concentration of NTR, was used in order to maximize the CEST effect. A CEST effect for the metal-bound water signal of **NO_2-Eu** was not observed, presumably because the carboxyl (CO_2H) protons undergo faster water exchange with bulk water (Figure S21). Electron delocalization from the ligand oxygen donor to the lanthanide ion decreases

along the series (carboxylate> amide> ketone), resulting in the weakest Eu^{3+}-water interaction and relatively fast water exchange in the carboxylate system. Conversely, ketone-type ligands provide for the strongest Eu^{3+}-water interactions and the slowest water exchange rates. Systems containing amides occupy an intermediate position.[43]

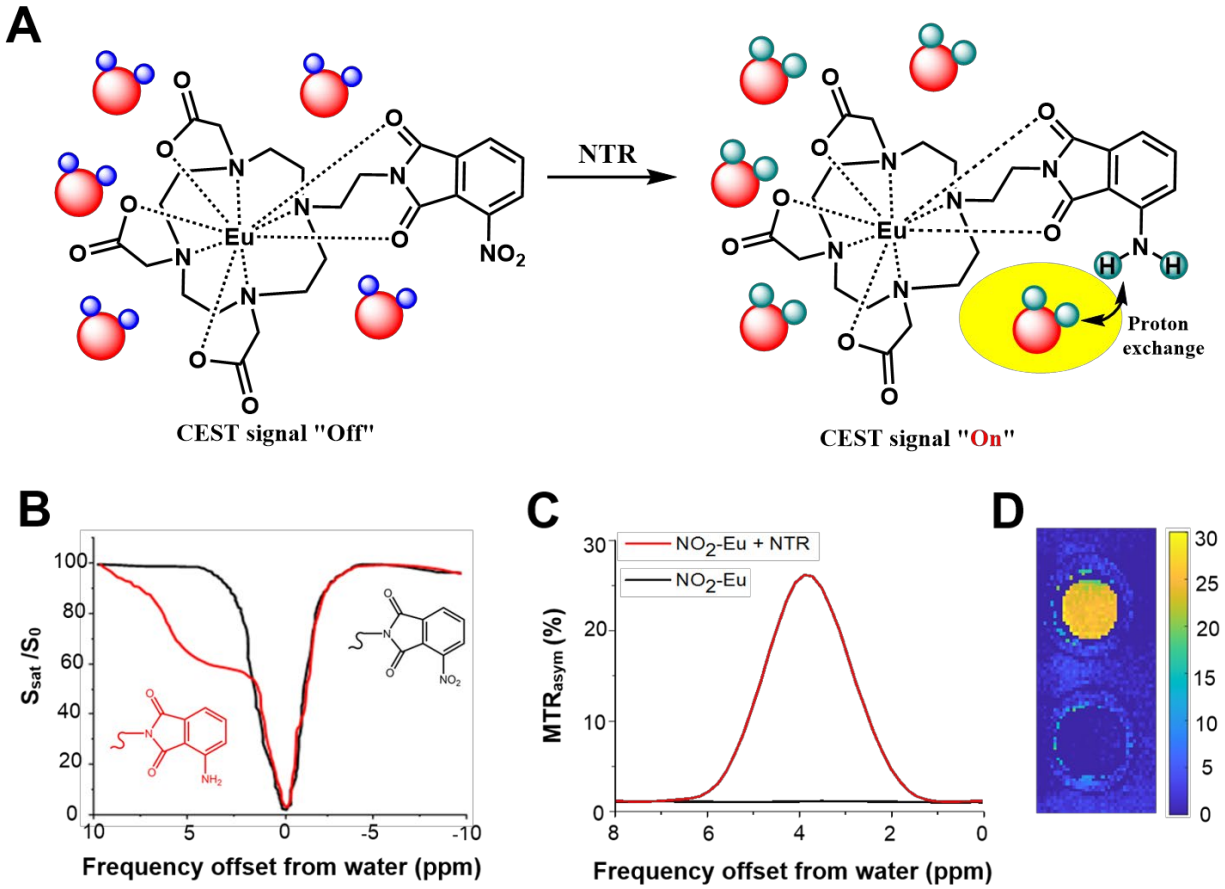

Figure 4. Schematic representation of the NTR activation process and *in vitro* CEST MRI detection of the bimodal probe NO_2-Eu. (A) Probe **NO_2-Eu** reduced by nitroreductase (NTR) contains exchangeable aniline NH_2 protons, and when these protons become RF-saturated, the surrounding water protons are also saturated, which turns on the CEST MRI signal. (B–D) At pH 7.4, the CEST spectrum of the reduced form of probe **NO_2-Eu** (20 mM, red line) was compared with the control (black line) using pre-saturated RF pulsing (B_1 = 4.0 μT, 2 s). The change in the CEST MRI signal is shown in the (B) Z-spectrum and (C) MTR_{asym} plots. (D) A representative CEST color map

(sum of the MTR_{asym} (%) values from 1.5 to 6 ppm in the presence (top) and absence (bottom) of NTR. All experiments were carried out in the presence of NADH (200 μM).

The NTR-dependent CEST spectrum for probe **NO_2-Eu** (20 mM) was then recorded in PBS at pH 7.4 using various concentrations of NTR (0, 10, 15, and 20 mM). As shown in Figure 5A, the CEST signals in the range of 2–6 ppm increased upon increasing the concentration of NTR, a finding attributed to greater quantities of the original 3-nitrophthalimide moiety being converted to the corresponding aniline form (i.e., 3-aminophthalimide). Ultimately, this results in enhanced proton exchange between the NH_2 protons and the bulk water protons.

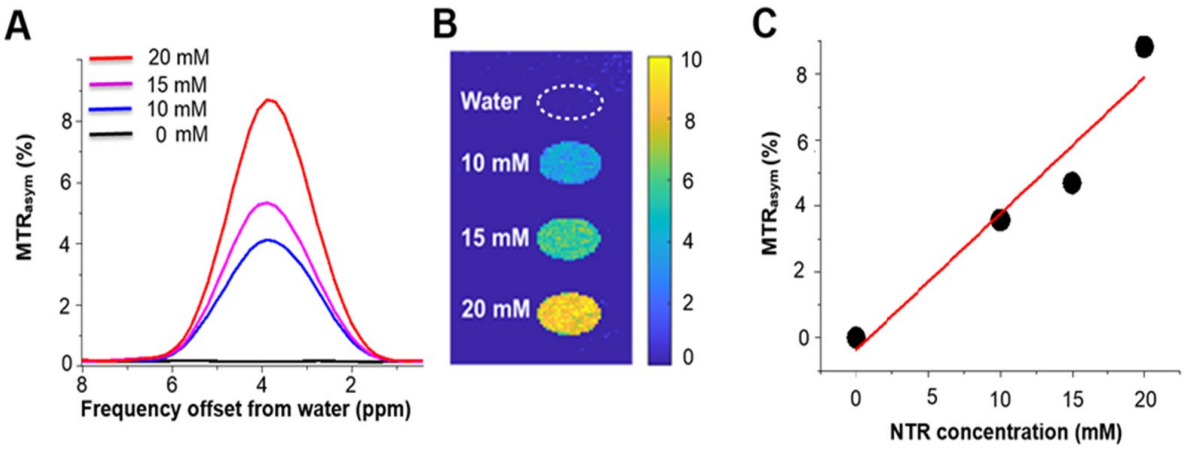

Figure 5. NTR concentration dependence on the CEST effect of probe NO_2-Eu. (A) MTR_{asym} (%) plot for probe **NO_2-Eu** (20 mM) as determined from experiments carried out following pre-incubation with various NTR concentrations (0, 10, 15, and 20 mM) in PBS for 5 min at 37°C and at pH 7.4. (B) A representative CEST color map at 4 ppm. (C) Calibration curve between the MTR_{asym} (%) value and the NTR concentration based on the color map. All experiments were carried out in the absence of NADH.

A CEST color map (Figure 5B) was constructed using the sum of the MTR_{asym} (%) values at 1.5–6 ppm. The NTR concentration-dependent MTR_{asym} (%) values at 4 ppm (Figures 5A) were also calibrated and plotted (Figure 5C), revealing a pseudolinear correlation between the NTR concentration and the CEST signal (R^2 = 0.967). It was found that the MTR_{asym} peak of ~9% at ~4 ppm for a 20 mM NTR concentration in the absence of the NADH coenzyme is about 1/3 of that measured with 200 μM NADH (Figure 5C). In order to explore further the kinetics of this enzyme-substrate reaction, a **NO_2-Eu (**substrate**)** concentration dependent CEST experiment with a fixed NTR (enzyme) concentration was also carried out. For this study, CEST spectra were recorded for various PBS probe **NO_2-Eu** (0, 10, 15, 20, 30 and 40 mM) solutions following pre-incubation with a fixed concentration of NTR (10 mM) for 60 min at pH 7.4 and at 37°C (Figure S22). As shown in Figure S22A, the CEST signals in the 2–6 ppm range increased upon increasing the concentration of **NO_2-Eu** up to about 40 mM. A CEST color map at 4 ppm (Figure S22B) and a quantitative comparison of the MTR_{asym} (%) values (Figure S22C) revealed a hyperbolic correlation between the NTR (enzyme) concentration and the CEST signal, and that the intensity of the CEST signal is almost saturated at 40 mM.

The CEST contrast of probe **NO_2-Eu** was found to be relatively sensitive to changes in the solution pH (Figure S23A), with the most intense signal being observed at pH = 7.5. In general, aromatic amine-based anticancer drugs show a CEST effect chemical shift in the 1-2 ppm range depending on the chemical structure.[44] In a solution, the pH is uniform throughout the medium, with the result that for **NO_2-Eu** the CEST signal depends first on activation by the enzyme (to give **NH_2-Eu**) with the chemical shift (Δw) then depending on intramolecular hydrogen bonding. NTR is active in the 5-9 pH range, but is maximally efficient at 7.4-7.5.[21,25,26] Once **NO_2–Eu** is activated, it is converted to NH_2–Eu, resulting in the CEST signal being turned "ON" per our design expectations and as highlighted in Scheme 1. The resulting 3-aminophthalimide-based compound **NH_2-Eu** is expected to support an intramolecular hydrogen bonding interactions between the amine (-NH_2) group and one or more carbonyl (C=O) moieties.[45-47] This results in a relatively slow k_{ex} at 7.4-7.5 pH giving rise, in turn, to a higher chemical shift CEST signal.[48] Both effects (NTR reduction and hydrogen bonding) are expected

to be favorable at pH ~7.5 and to act synergistically. This provides a rational for why a chemical shift at 4 ppm was observed at pH ~7.5. The CEST color map also revealed this pH dependence (Figure S23B). Maximum MTR_{asym} value was not monotonic with pH, and suddenly increased at pH 7.5 around ~4 fold from 7 to 27 with a chemical shift from ~2 ppm to ~4 ppm (Figure S23C), resulting from intramolecular hydrogen bonding of the 3-aminophthalimide group. The extent of carboxyl group protonation within the Eu-DOTA-tetraamide complex results in changes in the hydrogen bonding network, the proton exchange kinetics, and ultimately the strength of the CEST signal (Scheme S3).[49] In basic media, the ionized carboxyl groups (CO_2^-) can stabilize a strong hydrogen-bonding network involving bulk water molecules that slows prototropic exchange; therefore, a very strong CEST effect is observed under these conditions. Protonation of the carboxyl groups, as would be expected at neutral pH ~7, leads to a less-robust hydrogen bonding network, thereby allowing rapid proton exchange between the bulk water protons and the protons on the $–NH_2$ subunits. Finally, protonation of the $–NH_2$ groups in acidic media (pH <6) allow fast proton exchange, resulting in a very weak CEST effect.

In vitro CEST analysis in hypoxic tumor cells

We next recorded MTR_{asym} (%) curves for CT26 cells cultured in the presence and absence of probe **NO_2-Eu** (i.e., 0 and 10 mM). The CEST spectra (Figure 6A) were composed of two main peaks with a maximum at ~3 ppm, a finding attributed to the pH differences in the intra- and extra-cellular regions of the CT26 cells. The active form of the present CEST contrast agent contains exchangeable proton groups, such as $–NH_2$ and OH, and affords the opportunity for hydrogen bonding interactions. NTR also displays activity that varies with pH. Thus a pH-dependence is expected as noted above. However, when considering the use of **NO_2-Eu** *in vitro*, it is important to appreciate that there are different pH regions, such as extracellular and intracellular (cytosol, lysosome, ER, and other intra-cellular organelles) sub-spaces. As shown in Scheme S2, the CEST signal in a solution depends on only first proposed activation step (NTR-mediated reduction); however, *in vitro* and *in vivo*, the CEST signal is

expected to depend on both steps I and II. Indeed, a single peak in the CEST spectrum was recorded in PBS in the presence of the probe. In the MTR_{asym} spectra measured in PBS solution at pH 7.4 (Figures 4C and 5A), the MTR_{asym} peak is at ~4 ppm. In the pH-dependent MTR_{asym} spectra measured in PBS solution, the maximum peak depends on the pH value, in which the MTR_{asym} peaks at pH 5.5–7.0 and pH 8.0 are at ~2 ppm except at pH 7.5. These results are taken as evidence that the MTR_{asym} spectrum can fall in the 0 and >6 ppm range depending on the pH distribution of the regions.[50] In the precipitated CT26 cancer cells obtained following the NO_2-Eu treatment of this *in vitro* study, the pH distribution could cover the pH 4–7.5 range. The difference in effective extracellular (pH 6.3–6.9) and intracellular (at pH 4–7.5)[51] volumes would then result in the MTR_{asym} enhancement observed under hypoxic conditions (Figure 6A). Hypoxic CT26 cells, which express greater quantities of NTR than normoxic CT26 cells,[52,53] exhibited a significantly higher CEST signal (B_1 = 3.6 μT, 1 s) over a wide range of 1.5 to 6 ppm.

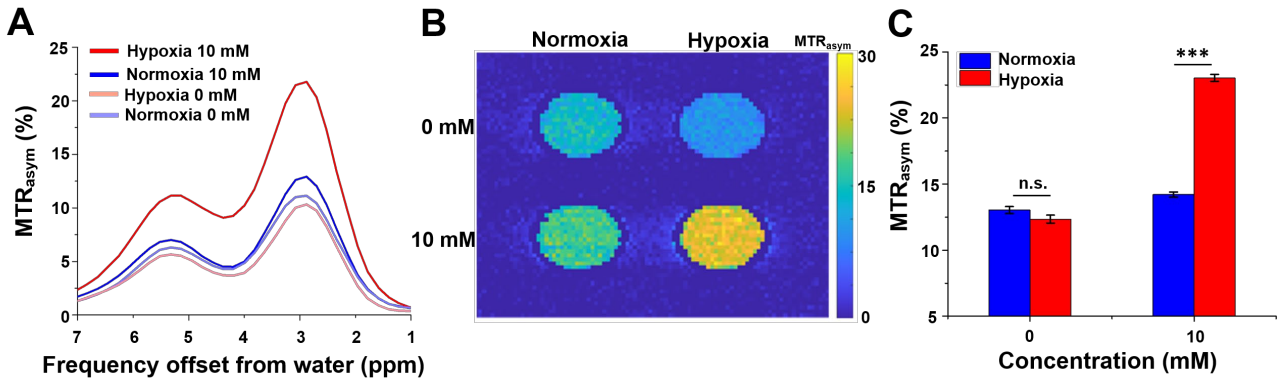

Figure 6. CEST imaging of CT26 cancer cells treated with probe NO_2-Eu. (A) CEST spectrum of CT26 cells incubated in the presence and absence of probe **NO_2-Eu** (0 or 10 mM) under hypoxic and normoxic conditions using a saturation field strength (i.e., B_1 = 3.6 μT, 1 s). (B) The CEST contrast color map at 3 ppm, and (C) a corresponding statistical comparison of signal intensities (SIs) determined from the color map. The data shown are averages of three experiments; the error bars represent the standard deviations. *P* values were determined using a nonpaired Student's t-test for homogenous variance. n.s., non-significant; ***$p < 0.001$.

In addition, the CEST color map generated at 3 ppm showed a distinctly enhanced CEST contrast under hypoxic conditions in the presence of probe **NO_2-Eu** (Figure 6B). Chemical shifts are affected by intramolecular hydrogen bonding of the 3-aminonaphthalimide moiety, which is correlated with the effective pH. Differences in the degree of intramolecular hydrogen bonding can result in a maximum between 2-4 ppm being reached depending on the pH value. Hypoxic tumors are acidic. As a consequence, fewer intramolecular hydrogen bonds are expected giving rise to a lower chemical shift (3 ppm) as seen by experiment. Based on CEST experiments involving independent CT26 cells (hypoxic and normoxic; n = 3 each) in the presence and absence of the probe (i.e., concentrations of 0 and 10 mM), the signal intensity in the hypoxic CT26 cells containing probe **NO_2-Eu** showed a significant contrast difference compared to the normoxic cells studied under otherwise identical conditions ($P = 0.001$); however, no significant enhancement was observed between the two normoxic conditions, i.e., in the presence and absence of the probe (Figure 6C). These results thus provide support for the core contention underlying the present study, namely that probe **NO_2-Eu** may be used to differentiate hypoxic tumor cells from normoxic cells *in vitro* as the result of differences in CEST enhancement.

In vivo CEST imaging of tumor hypoxia

We further investigated the suitability of probe **NO_2-Eu** for *in vivo* tumor detection and imaging as a CEST contrast agent in an animal tumor model. To demonstrate that probe **NO_2-Eu** can be used to detect tumor hypoxia, we performed *in vivo* CEST MR imaging of mice implanted with CT26 cells in the flank (Figure 7). CEST MR imaging with pre-saturation by an RF pulse (one hard pulse of B_1 = 3.6 μT, 1 s) before and after intra-tumoral (IT) injection of the probe (50 mM in PBS) was performed using a 4.7 T animal MRI system (Biospec 47/40, Bruker, Germany). We adjusted the pH to ~7.5 prior

to injecting a PBS solution of **NO_2-Eu** into the tumor site. Injected solution quickly equilibrates with its surroundings with regard to pH even when small amounts of acid or base solution are added externally. The effect of this injection is mostly affected by the NTR levels with high specificity thus being seen in the tumor site (Figures 2D and S14).

Accordingly, it has not proved possible to reach the mM concentrations needed for CEST MR imaging of the tumor site by intravenous injection.[54-56] It is a limitation of the present study that relatively higher **NO_2-Eu** (50 mM) needed to be used *in vivo*, due to the intrinsic low sensitivity of CEST MR. While beyond the scope of the present study, this limitation could be addressed by increasing the payload of the probe to improve the sensitivity (e.g., use of hydrogels, polymers, liposomes, exosomes, etc.).

Consistent with the solution and *in vitro* studies detailed above, relatively broad and strong CEST signals were observed at 0–5 ppm in the *in vivo* tumor region with higher intensity being seen 1 hr after **NO_2-Eu** (intra-tumoral) injection than for the pre-injection state (Figure S24). Biochemical and *in vitro* CEST MRI studies were performed at room temperature, whereas the *in vivo* studies were performed at 37°C. Lower temperatures reduce the rate of chemical exchange, resulting in better CEST signal enhancement. This is because amines usually exchange too quickly to produce a CEST effect as evidenced by the fact that the CEST effect increases as the exchange rate of the amine protons decreases.

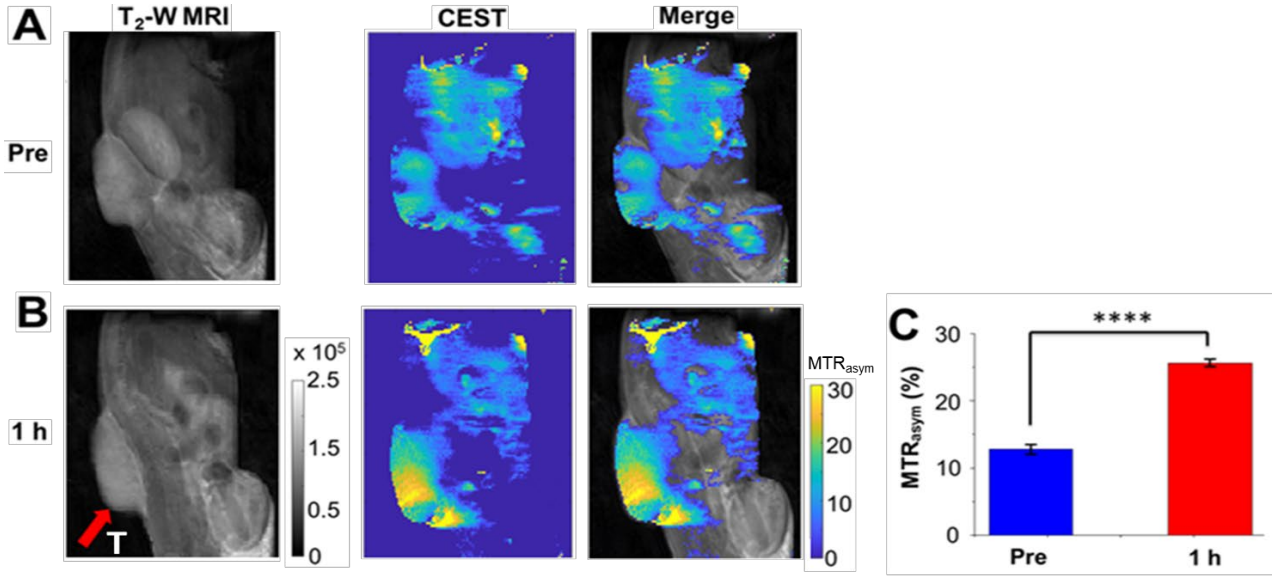

Figure 7. ***In vivo CEST imaging of probe NO_2-Eu in a CT26 xenograft mouse model.*** T_2-W and CEST MR images were obtained (A) before and (B) 1 h after intra-tumoral injection (n = 3) of probe **NO_2-Eu** (50 mM, 100 μL) in PBS for a CT26 tumor-bearing mouse (tumor diameter d ~10 mm). Each CEST MR image recorded at 2.5 ppm was merged with the corresponding T_2-W MR image. (C) Quantitative comparison of the mean MTR_{asym} (%) values at 2.5 ppm for the tumor region. The data shown are averages of three measurements; the error bars show the standard deviations. *P* values were determined using a nonpaired Student's t-test for homogenous variance. ****, $p < 0.0001$.

The T_2-W, CEST, and merged images are shown in Figures 7A and 7B for the CT26 tumor xenograft mice before and 1 h after injection of probe **NO_2-Eu**. Following IT injection of the probe, a CEST signal enhancement at 2.5 ppm was observed mainly around the injection site within the tumor area (T), a finding attributed to selective activation of the nitro group present in probe NO_2-Eu at the tumor site. The MTR_{asym} (%) value at 2.5 ppm within the tumor region increased ~2-fold 1 h after injection of probe **NO_2-Eu** (Figure 7C). We take these findings as evidence that the CEST signal was enhanced following probe injection and that tumor hypoxia serves to promote "switching on" of probe **NO_2-Eu**.

In the present study, the whole tumor area was considered as the region-of-interest to measure MTR_{asym}, because it proved impossible to select reliably only the hypoxic tumor core region.

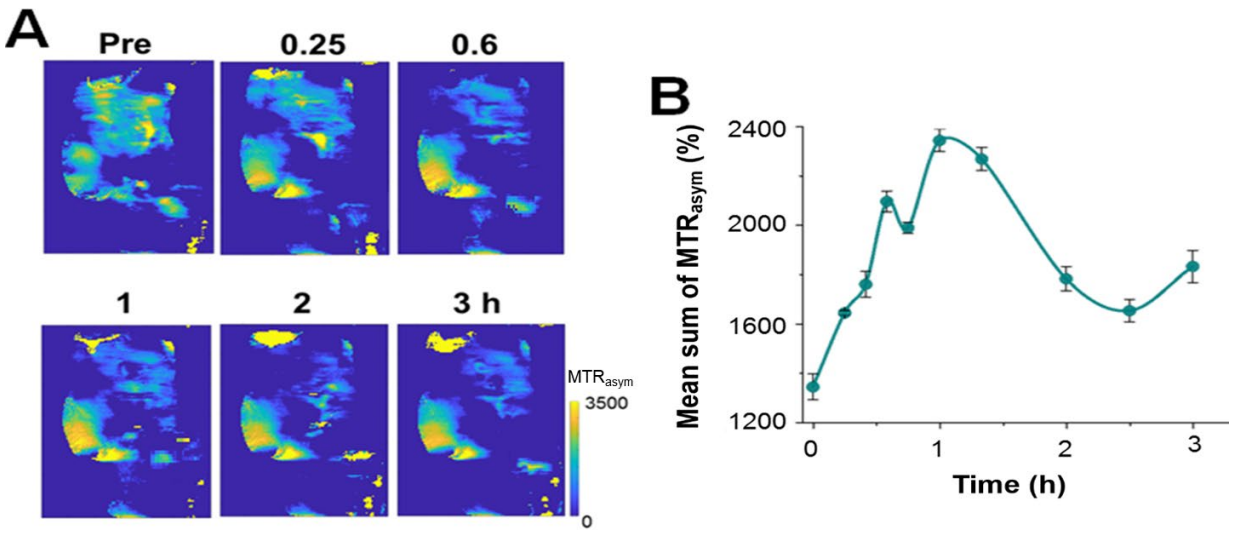

Figure 8. Time dependent *in vivo* CEST imaging of probe NO_2-Eu. (A) Time dependent *in vivo* CEST images were recorded for a CT26 tumor-bearing mouse before and after intra-tumoral injection (n = 3) of **NO_2-Eu** (50 mM, 100 μL) in PBS. The CEST images were obtained using sum of the MTR_{asym} (%) values recorded between 1.5 and 5 ppm. (B) Dynamic plot of the mean CEST intensity over the entire tumor region versus time following injection of probe **NO_2-Eu**. This region corresponded to that shown in Figure S15D.

The *in vivo* CEST signal changes were monitored for up to 3 h following injection of probe **NO_2-Eu**. Figure 8A shows the change in the CEST MRI signal (sum of the MTR_{asym} (%) values between 1.5 and 5 ppm) over time. As can be seen from an inspection of this figure, immediately after injection of the probe, the CEST MR signals close to the injection site within the tumor region began to increase in intensity before the enhancement gradually spreads to the surroundings. The mean CEST signals observed in Figure 8A were measured over the entire tumor area at 10 time points before and after injecting probe **NO_2-Eu** (Figure 8B). While the CEST signals could be observed 0.25 h post-injection, the greatest signal intensity was observed after 1 h. The signals were still observable after 3 h. The

MTR_{asym} (%) values at 2.5 ppm were also analyzed, and similar results were obtained (Figure S25). These results lead us to conclude that probe **NO_2-Eu** was selectively activated by hypoxia-driven NTR in the tumor region and that once administered, it moves out from the point of initial injection.

■ CONCLUSIONS

We have described here a dual action "switch on" emissive and CEST MRI sensor for hypoxic environments. The system in question, probe NO_2-Eu, consists of a 3-nitrophthalimide-functionalized Eu^{3+} DOTA derivative that is activated by NTR. Activation of the probe was NTR-specific, with no interference being observed in the presence of a range of potential biologically relevant interferants, such as various anions, enzymes, amino acids, and vitamins. We also found that probe **NO_2-Eu** is applicable *in vivo* and could be used to monitor hypoxic regions within a CT26 mouse xenograft via the production of both an NTR-specific luminescence signal and CEST MR imaging. We thus suggest that dual action probes such as the one described here may have a role to play in both *in vitro* and *in vivo* hypoxia imaging studies.

■ EXPERIMENTAL SECTION

Materials, methods and instrumentations

Analytical grade chemicals were obtained commercially and used without further purification unless otherwise indicated. Further details, including the synthesis of compounds **2**-**4** are provided in the Supporting Information. All compounds are >95% pure by HPLC analysis.

Absorption and luminescence studies

Fluorescence emission and UV-vis spectra were recorded using an S-3100 spectrophotometer (Scinco, Seoul, Korea) and a standard 1 cm quartz cell and a UV-1800 spectrophotometer (Scinco), respectively. Nitroreductase (NTR) from *Escherichia coli* was used in the present studies. Stock solutions of various analytes (NADH, KCl, $CaCl_2$, $MgCl_2$, glucose, vitamin C, 1 mM vitamin B6, HSA, H_2O_2, ·OH (•OH) was generated by irradiation of 10 mM $NaNO_2$ solution with UV-A light (354 ± 20 nm), glutamic acid, arginine, serine, glutathione, cysteine, homocysteine, and dithiothreitol) were prepared using double distilled water. A stock solution of probe **NO_2-Eu** (25 μM) was prepared using Dulbecco's Modified Eagle Medium (DMEM) containing 10% FBS (pH 7.4) and 0.2% DMSO. The fluorescent spectra were measured using an excitation wavelength of 405 nm and a 5 nm slit width. The change in the emission features of probe **NO_2-Eu** (5.0 μM) were recorded in the absence and presence of NTR (0-1 μg/ml). The fluorescence quantum yield of the probe was measured in the presence or absence of NTR in cell media (pH 7.4).

Cell viability assay and flow cytometry

To evaluate the cytotoxicity of the **NO_2-Eu**, CT26 cells were seeded at a density of 20,000 cells/well in 96 well plates. The next day, for the studies involving hypoxic conditions, the cells were transferred to a hypoxic (O_2 < 0.1%) chamber (STEMCELL Technologies, Inc., Vancouver, BC, Canada) and cultured for 24 h before probe treatment. The cells were then incubated with various **NO_2-Eu** concentrations (0, 0.25, 0.5, and 1 mM) for 3 h, or with 2.5, 5, 10, and 20 mM of **NO_2-Eu** for 24 h under hypoxic or normoxic conditions. Cell viability was determined using a cell proliferation kit

(Celltiter96; Promega Corporation, Madison, WI, USA) following the manufacturer's instructions. The absorbance was measured using a microplate reader (XMark, Bio-Rad, Berkeley, CA, USA) at 490 nm.

Cultured *E. coli* was centrifuged at 4,000 rpm for 10 min. The resulting pellets were resuspended in PBS. The pellets were redissolved in the culture medium and then treated with 0, 0.5, or 1 mM of probe **NO_2-Eu** for 1 h at 37°C with agitation (200 rpm). After incubation, the cells were harvested and washed two times with PBS and then transferred to flow cytometry tubes.

CT26 cells were seeded at a density of 1.5×10^5 cells/well in 6-well plates, and were allowed to grow overnight. The cells were then pre-incubated for 24 h under hypoxic (O_2 < 1%) or normoxic conditions prior to incubation with the **NO_2-Eu** (0.5 mM, 1 mM) probe. After incubation for 10 min to 3 h, the cells were gently scraped, suspended in PBS (Gibco), and transferred to flow cytometry tubes. Subsequently, the cells were analyzed using a flow cytometer (CytoFLEX; Beckman Coulter) using the KO525 channel (405 nm excitation, 525/40 nm emission). All analyses were carried out at least three times using at least 10,000 cells.

***In vitro* cell imaging**

CT26 cells were seeded at a density of 2×10^4 cells/well in eight-well plates at 37°C in a 5% CO_2 incubator overnight. The cells were transferred to a hypoxia (1% O_2) chamber or kept under normoxic condition for 24 h, and then incubated with 20 μM **NO_2-Eu** for 30 min. Lminescence images were obtained using a fluorescence microscope (Olympus IX81, 400×) equipped with GFP filter set. Fluorescence images were acquired using a confocal laser scanning fluorescence microscope (LSM710, Carl Zeiss, Oberkochen, Germany) equipped with a FITC filter set. For the fluorescence imaging studies involving CT26 cells, the cells were seeded at a density of 2×10^4 cells/well in eight-well plates (Ibidi, Martinsried, Germany) at 37ºC in a humidified incubator and kept overnight. The next day, the

cells were transferred to a hypoxia (1 % O_2) incubator chamber or kept under normoxic conditions for 24 h and then incubated with 0.5 mM **NO_2-Eu** for either 20 min or 60 min.

Sample preparation for CEST imaging

Various solution phantoms were made up using 20 mM solutions of the **NO_2-Eu**. These included samples with or without NTR (20 mM) for CEST efficiency measurements, samples with different NTR concentrations (0, 10, 15, and 20 mM), and samples of various pH (5.5, 6.0, 6.5, 7.0, 7.5, and 8.0) with NTR (20 mM) for pH dependency measurements. Each sample was prepared in a PCR tube (200 μL), and then placed inside a 50 mL conical tube filled with water.

CT20 cells were seeded (5×10^6 cells) in 100 mm culture dish (Ibidi, Martinsried, Germany) at 37°C in a humidified incubator, and kept overnight. The next day, the cells were transferred to a hypoxic ($O_2 < 0.1\%$) chamber or kept under normoxic conditions for 24 h. They were then incubated with probe **NO_2-Eu** (0 mM or 10 mM) for 15 min. The cells were then harvested at 1,500 rpm for 15 minutes, and washed two times with DPBS. Finally, the cells were resuspended in DPBS, transferred to PCR tubes, and precipitated.

MRI studies

MRI experiments were performed on a 4.7 T animal MRI system (Biospec 47/40, Bruker, Germany) with a 35 mm volume transceiver coil. All MR images were acquired using the ParaVision 5.1 (Bruker, Germany) software using a modified rapid acquisition with relaxation enhancement (RARE) sequence for the CEST experiments. CEST-weighted MR images were acquired with the following parameters: field of view (FOV) = 4×3 mm^2, slice thickness = 2 mm, matrix size = 128×128, TE/TR = 7.7 ms / 5 s, total acquisition time = 5 min 15 s, and RARE factor = 128, including a pre-saturation RF pulse (one hard pulse, B_1 = 4.0 μT, 2s or 3.6 μT, 1s) from -10 to 10 ppm (step of 0.3 ppm). A water saturation

shift referencing (WASSR) scheme for B_0 homogeneity correction was used.[57] The same parameters as used for the CEST imaging were used for all CEST experiments except TR = 2 sec, total acquisition time = 2 min 6 s, and pre-saturation RF pulse (one hard pulse, B_1 = 0.2 μT, 0.5 s) from -1 ppm to 1 ppm (step = 0.03 ppm).

All animal experiments were performed according to protocols approved by the Institutional Animal Care and Use Committee of the Korean Basic Sciences Institute (KBSI-AEC-1902). A mouse tumor model was established by injecting CT26 cells (5×10^5 cells per mouse) subcutaneously into the flank region of 6-week-old male mice (Balb/c-nude, n = 4). 10–12 days after tumor inoculation, probe **NO_2-Eu** (50 mM) dissolved in PBS (100 μl) was injected intratumorally to the selected mice (n = 3) with appropriate tumor size, and *in vivo* CEST images were acquired before and 15, 25, 35, 45, 60, 80, 120 and 180 min after intratumoral (IT) injection of the **NO_2-Eu**.

MRI data analysis

MRI data were processed using a custom-written program in Matlab (Mathworks, Natick, MA, USA). In order to measure the voxel-by-voxel frequency shift caused by B_0 inhomogeneity, a WASSR map was generated, and CEST signals at each voxel were corrected using the WASSR map. Then, the CEST spectra were calculated from the mean of the region-of-interests (ROIs) on a per-voxel basis. The CEST map was quantified using the magnetic transfer asymmetry ratio, MTR_{asym}(%), at particular offsets of interest using the definition: MTR_{asym} (%) = $(S_{-\Delta\omega} - S_{+\Delta\omega}) \times 100 / S_0$, where $S_{-\Delta\omega}$, $S_{+\Delta\omega}$ and S_0 are the water signal intensity under saturation pulses at offsets of $-\Delta\omega$ and $+\Delta\omega$, respectively. All studies were carried out at room temperature.

■ ASSOCIATED CONTENT

Supporting Information

The Supporting Information is available free of charge at https://pubs.acs.org/doi/???; including supporting materials and methods, figures, tables, and spectroscopic data of compounds (Word); Molecular formula strings (CSV).

■ AUTHOR INFORMATION

Corresponding Authors

Kwan Soo Hong – *Research Center for Bioconvergence Analysis, Korea Basic Science Institute, Cheongju 28119, Korea; Graduate School of Analytical Science and Technology, Chungnam National University, Daejeon 34134, Korea; ORCID: 0000-0003-4342-5183; Email: kshong@kbsi.re.kr*

Jonathan L. Sessler – *Department of Chemistry, The University of Texas at Austin, Austin, Texas 78712-1224, USA; ORCID: 0000-0002-9576-1325; Email: sessler@cm.utexas.edu*

Jee-Hyun Cho – *Research Equipment Operations Division, Korea Basic Science Institute, Cheongju 28119, Korea*; Email: jhcho@kbsi.re.kr

Authors

Sanu Karan – *Research Center for Bioconvergence Analysis, Korea Basic Science Institute, Cheongju 28119, Korea; Graduate School of Analytical Science and Technology, Chungnam National University, Daejeon 34134, Korea; ORCID: 0000-0002-1119-2314*

Mi Young Cho – *Research Center for Bioconvergence Analysis, Korea Basic Science Institute, Cheongju 28119, Korea; ORCID: 0000-0003-0676-7635*; Present address: *SKKU Advanced*

Institute of Nanotechnology (SAINT), School of Chemical Engineering, Sungkyunkwan University, Suwon 16419, Korea

Hyunseung Lee - *Research Center for Bioconvergence Analysis, Korea Basic Science Institute, Cheongju 28119, Korea*; ORCID: 0000-0002-4506-9602

Hye Sun Park – *Research Center for Bioconvergence Analysis, Korea Basic Science Institute, Cheongju 28119, Korea*; ORCID: 0000-0002-3275-1437

Eun Hee Han – *Research Center for Bioconvergence Analysis, Korea Basic Science Institute,Cheongju 28119, Korea*; ORCID: 0000-0002-0137-0156

Youngkyu Song – *Research Equipment Operations Division, Korea Basic Science Institute, Cheongju 28119, Korea*

Youlee Lee – *Research Equipment Operations Division, Korea Basic Science Institute,Cheongju 28119, Korea*

Mina Kim – *Department of Neuroinfammation, Faculty of Brain Sciences, UCL Queen Square Institute of Neurology, London WC1N 3BG, UK*

Author Contribution

The manuscript was written through the contribution of all authors. All authors have given approval to the final version of the manuscript. SK and MYC contributed equally to this study.

Notes

The authors declare no competing financial interest.

■ ACKNOWLEDGMENTS

This work was supported by the National Research Council of Science and Technology (NST) grant from the Korea government (MSIT) (KSH, CAP-18-02-KRIBB), the National Research Foundation of Korea (NRF) grant funded by the Korea government (MSIT) (KSH, 2020R1A2C2012011), and Korea Basic Science Institute grant (JHC, C130000). The work in Austin was supported by the Robert A. Welch Foundation (F-0018 to JLS).

■ ABBREVIATIONS

CEST, chemical exchange saturation transfer; CYCLEN, 1,4,7,10-tetraazacyclododecane; DMF, dimethylformamide; DMEM, dulbecco's modified eagle medium; DMSO, dimethyl sulfoxide; DOTA, 1,4,7,10-tetraazacyclododecane-1,4,7,10-tetraacetic acid; E_m, emission; E_x, excitation; EtOAc, ethyl acetate; FBS, fetal bovine serum; Hex, hexanes; HPLC, high performance liquid chromatography; HRMS, high resolution mass spectrometry; ICT, intramolecular charge transfer; IT, Intra-tumoral; *J*, coupling constant (in NMR spectrometry); MRI, magnetic resonance imaging; MS, mass spectrometry; MTR, magnetization transfer ratio; *m*/*z*, mass-to-charge ratio; NADH, reduced nicotinamide adenine dinucleotide; NBS, *N*-bromosuccinimide; TFA, trifluoroacetic acid.

■ REFERENCES

(1) Koh, Y. M.; Powis, G. Passing the baton: The HIF switch. *Cell* **2012**, *37*, 364–372.

(2) Harris, A. L. Hypoxia — a key regulatory factor in tumour growth. *Nat. Rev. Cancer* **2002***, 2,* 38–47.

(3) Semenza, G. L. Targeting HIF-1 for cancer therapy. *Nat. Rev. Cancer* **2003**, *3*, 721–732.

(4) Qayum, N.; Muschel, R. J.; Im, J. H.; Balathasan, L.; Koch, J. C.; Patel, S.; McKenna, W. G.; Bernhard, E. J. Tumor vascular changes mediated by inhibition of oncogenic signaling. *Cancer Res.* **2009**, *69*, 6347–6354.

(5) Vaupel, P.; Schlenger, K.; Knoop, C.; Hockel, M. Oxygenation of human tumors: evaluation of tissue oxygen distribution in breast cancers by computerized O_2 tension measurements. *Cancer Res.* **1991**, *51*, 3316–3322.

(6) Grimes, D.R.; Fletcher, A.G.; Partridge, M. Oxygen consumption dynamics in steady-state tumour models. *R. Soc. Open Sci.* **2014**, *1*, 140080.

(7) Brown, J. M.; Wilson, W. R. Exploiting tumour hypoxia in cancer treatment. *Nat. Rev. Cancer* **2004**, *4*, 437–447.

(8) Brown, J. M. Clinical trials of radiosensitizers: what should we expect? *Int. J. Radiat. Oncol. Biol. Phys.* **1984**, *10*, 425–429.

(9) Koch, C. J. Oxygen effects in radiobiology. *Adv. Exp. Med. Biol.* **1982**, *157*, 123–144.

(10) Dewhirst, M. W.; Cao, Y.; Moller, B. Cycling hypoxia and free radicals regulate angiogenesis and radiotherapy response. *Nat. Rev. Cancer* **2008**, *8*, 425–427.

(11) Codony, V. L.; Tavassoli, M. Hypoxia-induced therapy resistance: available hypoxia-targeting strategies and current advances in head and neck cancer. *Transl. Oncol.* **2021**, *14*, 101017.

(12) Peraz-Herrero, E.; Fernandez-Medarde, A. The reversed intra- and extracellular pH in tumors as a unified strategy to chemotherapeutic delivery targeted nanocarriers. *Acta Pharm. Sin. B* **2021**, *11*, 2243–2264.

(13) Price, J. M.; Robinson, S. P.; Koh, D. M. Imaging hypoxia in tumours with advanced MRI. *Q. J. Nucl. Med. Mol. Imaging* **2013**, *57*, 257–270.

(14) Dewhirst, M. W.; Birer, S. R. Oxygen-enhanced MRI is a major advance in tumor hypoxia imaging. *Cancer Res.* **2016**, *76*, 769–772.

(15) Fleming, I. N.; Manavaki, R.; Blower, P. J.; West, C.; Williams, K. J.; Harris, A. L.; Domarkas, J.; Lord, S.; Baldry, C.; Gilber, F. J. Imaging tumour hypoxia with positron emission tomography. *Br. J. Cancer* **2015**, *112*, 238–250.

(16) Xu, K.; Wang, F.; Pan, X.; Liu, R.; Ma, J.; Kong, F.; Tang, B. High selectivity imaging of nitroreductase using a near-infrared fluorescence probe in hypoxic tumor. *Chem. Commun*. **2013**, *49*, 2554–2556.

(17) Elmes, R. B. P. Bioreductive fluorescent imaging agents: applications to tumour hypoxia. *Chem. Commun.* **2016**, *52*, 8935–8956.

(18) Hodgkiss, R. J.; Jones, G. W.; Long, A.; Middleton, R. W.; Parrick, J.; Stratford, M. R.; Wardman, P.; Wilson, G. D. Fluorescent markers for hypoxic cells: a study of nitroaromatic compounds, with fluorescent heterocyclic side chains, that undergo bioreductive binding. *J. Med. Chem.* **1991**, *34***,** 2268–2274.

(19) Tanabe, K.; Hirata, N.; Harada, H.; Hiraoka, M.; Nishimoto, S. Emission under hypoxia: one-electron reduction and fluorescence characteristics of an indolequinone-coumarin conjugate. *Chem. Biochem.* **2008**, *9***,** 426–432.

(20) Sandhu, S.; Kydd, L.; Jaworski, J. Luminescent probe based techniques for hypoxia imaging. *J. Nanomed. Res.* **2017,** *6*, 00160.

(21) Karan, S.; Cho, M. Y.; Lee, H.; Lee, H.; Park, H. S.; Sundarajan, M.; Sessler, J. L.; Hong, K. S. Near-infrared fluorescent probe activated by nitroreductase for In vitro and in vivo hypoxic tumor detection. *J. Med. Chem.* **2021**, *64*, 2971–2981.

(22) Li, Y.; Sun, Y.; Li, J.; Su, Q.; Yuan, W.; Dai, Y.; Han, C.; Wang, Q.; Feng, W.; Li, F. Ultrasensitive near-infrared fluorescence-enhanced probe for in vivo nitroreductase imaging. *J. Am. Chem. Soc.* **2015**, *137*, 6407–6416.

(23) Zheng, X.; Wang, X.; Mao, H.; Wu, W.; Liu, B.; Jiang, X. Hypoxia-specific ultrasensitive detection of tumours and cancer cells in vivo. *Nat. Commun*. **2015**, *6*, 5834.

(24) Knox, H. J.; Hedhli, J.; Kim, T. W.; Khalili, K.; Dobrucki, L. W.; Chan, J. A bioreducible N-oxide-based probe for photoacoustic imaging of hypoxia. *Nat. Commun*. **2017**, *8*, 1794.

(25) Zheng, J.; Shen, Y.; Xu, Z.; Yuan, Z.; He, Y.; Wei, C.; Er, M.; Yin, J.; Chen, H. Near-infrared off-on fluorescence probe activated by NTR for in vivo hypoxia imaging. *Biosens. Bioelectron*. **2018**, *119*, 141–148.

(26) Li, Z.; Gao, X.; Shi, W.; Li, X.; Ma, H. 7-((5-Nitrothiophen-2-yl)methoxy)-3H-phenoxazin-3-one as a spectroscopic off-on probe for highly sensitive and selective detection of nitroreductase. *Chem. Commun.* **2013**, *49*, 5859–5861.

(27) Wong, R. H.; Kwong, T.; Yau, K.-H.; Au-Yeung, H. Y. Real time detection of live microbes using a highly sensitive bioluminescent nitroreductase probe. *Chem. Commun*. **2015**, *51*, 4440–4442.

(28) Zhu, D.; Xue, L.; Li, G.; Jiang, H. A highly sensitive near-infrared ratiometric fluorescent probe for detecting nitroreductase and cellular imaging. *Sens. Actuators B Chem.* **2016**, *222*, 419–424.

(29) Lauffer, R. B. Paramagnetic metal complexes as water proton relaxation agents for NMR imaging: theory and design. *Chem. Rev.* **1987**, *87*, 901–927.

(30) Pierre, V. C.; Allen, M. J.; Caravan, P. Contrast agents for MRI: 30+ years and where are we going. *J. Biol. Inorg. Chem.* **2014**, *19*, 127–131.

(31) Verwilst, P.; Park, S.; Yoon, B.; Kim, J. S. Recent advances in Gd-chelate based bimodal optical/MRI contrast agents. *Chem. Soc. Rev.* **2015**, *44*, 1791–806.

(32) Forsen, S. Study of moderately rapid chemical exchange reactions by means of nuclear magnetic double resonance. *J. Chem. Phys.* **1963**, *39*, 2892.

(33) Ratnakar, S. J.; Viswanathan, S.; Kovacs, Z.; Jindal, A. K.; Green, K. N.; Sherry, A. D. Europium(III) DOTA-tetraamide complexes as redox-active MRI sensors. *J. Am. Chem. Soc.* **2012**, *134*, 5798–5800.

(34) Yoo, B.; Pagel, M. D. A PARACEST MRI contrast agent to detect enzyme activity. *J. Am. Chem. Soc.* **2006**, *128*, 14032–14033.

(35) Ratnakar, S. J.; Chirayil, S.; Funk, A. M.; Zhang, S.; Queiró, J. F.; Geraldes, C. F. G. C.; Kovacs, Z.; Sherry, A. D. A frequency-selective pH-responsive paraCEST agent. *Angew. Chem. Int. Ed.* **2020**, *59*, 21671–21676.

(36) Wang, X.; Wu, Y.; Soesbe, T. C.; Yu, J.; Zhao, P.; Keifer, G. E.; Sherry, A. D. A pH-responsive MRI agent that can be activated beyond the tissue magnetization transfer window. *Angew. Chem. Int. Ed.* **2015**, *54*, 8862–8664.

(37) Funk, A. M. Jordan, V. C.; Sherry, A. D.; Ratnakar, S. J.; Kovacs, Z. Oxidative conversion of a europium(II)-based T1 agent into a europium(III)-based paraCEST agent that can be detected *in vivo* by magnetic resonance imaging. *Angew. Chem. Int. Ed.* **2016**, *55*, 5024–5027.

(38) Zhang, L.; Martins, A. F.; Zhao, P.; Wu, Y.; Tircso, G.; Sherry, A. D. Lanthanide-based T_{2ex} and CEST complexes provide insights into the design of pH Sensitive MRI Agents. *Angew. Chem. Int. Ed.* **2017**, *56*, 16626–16630.

(39) Wu, J. Martins, A. F.; Preihs, C.; Jordan, V. C.; Chirayil, S.; Zhao, P.; Wu, Y.; Nasr, K.; G. E. Kiefer, G. E.; Sherry, A. D. Amplifying the sensitivity of zinc(II) responsive MRI contrast agents by altering water exchange rates. *J. Am. Chem. Soc.* **2015**, *137*, 14173–14179.

(40) Zhang, H.; Liu, J.; Liu, C.; Yu, P.; Sun, M.; Yan, X.; Guo, J. P.; Guo, W. Imaging lysosomal highly reactive oxygen species and lighting up cancer cells and tumors enabled by a Si-rhodamine-based near-infrared fluorescent probe. *Biomaterials* **2017**, *133*, 60–69.

(41) Xu, K. H.; Qiang, M. M.; Gao, W.; Su, R. X.; Li, N.; Gao, Y.; Xie, Y. X.; Kong, F. P.; Tang, B. A near-infrared reversible fluorescent probe for real-time imaging of redox status changing in vivo. *Chem. Sci*. **2013**, *4*, 1079–1086.

(42) Xiao, B. H.; Li, P.; Zhang, S.; Zhang, W.; Tang, B. Simultaneous fluorescence visualization of mitochondrial hydrogen peroxide and zinc ions in live cells and in vivo. *Chem. Commun.* **2016**, *52*, 12741–12744.

(43) Hancu, I.; Dixon, W. T.; Woods, M.; Vinogradov, E.; Sherry, A. D.; Lenkinski, R. E. CEST and PARACEST MR contrast agents. *Acta radiol.* **2010**, *51*, 910–923.

(44) Li, Y.; Chen, H.; Xu, J.; Yadav, N. N.; Chan, K. W.; Luo, L.; McMahon, M. T.; Vogelstein, B.; van Zijl, P. C.; Zhou, S.; Liu, G. CEST theranostics: label-free MR imaging of anticancer drugs. *Oncotarget* **2016**, *7*, 6369–6378.

(45) Yang, L.; Liu, X.; Gao, L.; Qi, F.; Tian, H.; Song, X. A selective and sensitive phthalimide-based fluorescent probe for hydrogen sulfide with a large stokes shift. *RSC Adv.* **2015**, *5*, 98154–98159.

(46) Wang, D.; Bai, T.; Wang, X.; Xiong, Y.; Zhang, Y.; Shi, Z.; Qing, G. Sensing mechanism of excited-State intermolecular hydrogen bond for phthalimide: indispensable role of dimethyl sulfoxide. *Chin. J. Chem.* **2021**, *39*, 1113–1120.

(47) Vogt, N.; Savelev, D.; Giricheva, N. I.; Girichev, G. V. Accurate equilibrium structure of 3-aminophthalimide from gas electron diffraction and coupled-cluster computations and diverse structural effects due to electron density transfer. *Phys. Chem. Chem. Phys.* **2020**, *22*, 27539–27546.

(48) Yang, X.; Song, X.; Ray Banerjee, S.; Li, Y.; Byun, Y.; Liu, G.; Bhujwalla, Z. M.; Pomper, M. G.; McMahon, M. T. Developing imidazoles as CEST MRI pH sensors. *Contrast media mol. imaging* **2016**, *11*, 304–312.

(49) Zhang, L.; Evbuomwan, O. M.; Tieu, M.; Zhao, P.; Martins, A. F.; and Sherry, A. D. Protonation of carboxyl groups in Eu-DOTA-tetraamide complexes results in catalytic prototropic exchange and quenching of the CEST signal. *Philos. Trans. A Math. Phys. Eng. Sci*. **2017**, *375*, 20170113.

(50) Jamin, Y.; Eykyn, T. R.; Poon, E.; Springer, C. J.; Robinson, S. P. Detection of the prodrug-activating enzyme carboxypeptidase G2 activity with chemical exchange saturation transfer magnetic resonance. *Mol. Imaging biol.* **2014**, *16*, 152–157.

(51) Mowday, A. M.; Copp, J. N.; Syddall, S. P.; Dubois, L. J.; Wang, J.; Lieuwes, N. G.; Biemans, R.; Ashoorzadeh, A.; Abbattista, M. R.; Williams, E. M.; Guise, C. P.; Lambin, P.; Ackerley, D.

F.; Smaill, J. B.; Theys, J.; and Patterson, A. V. *E. coli* nitroreductase NfsA is a reporter gene for non-invasive PET imaging in cancer gene therapy applications. *Theranostics* **2020**, *10*, 10548–10562.

(52) Fan, L.; Zan, Q.; Lin, B.; Wang, X.; Gong, X.; Zhao, Z.; Shuang, S.; Dong, C.; and Wong, M. S. Hypoxia imaging in living cells, tissues and zebrafish with a nitroreductase-specific fluorescent probe. *Analyst* **2020**, *145*, 5657–5663.

(53) Jin, H. S.; Choi, D. S.; Ko, M.; Kim, D.; Lee, D. H.; Lee, S.; Lee, A. Y.; Kang, S. G.; Kim, S. H.; Jung, Y.; Jeong, Y.; Chung, J. J.; Park, Y. Extracellular pH modulating injectable gel for enhancing immune checkpoint inhibitor therapy. *J. Control. Release* **2019***, 315*, 65–75.

(54) Chen, Z.; Li, Y.; Airan, R.; Han, Z.; Xu, J.; Chan, K.; Xu, Y.; Bulte, J.; van Zijl, P.; McMahon, M. T.; Zhou, S.; and Liu, G. CT and CEST MRI bimodal imaging of the intratumoral distribution of iodinated liposomes. *Quant. Imaging Med. Surg.* **2019**, *9*, 1579–1591.

(55) Brachi, G.; Ruiz-Ramírez, J.; Dogra, P.; Wang, Z.; Cristini, V.; Ciardelli, G.; Rostomily, R. C.; Ferrari, M.; Mikheev, A. M.; Blanco, E.; and Mattu, C. Intratumoral injection of hydrogel-embedded nanoparticles enhances retention in glioblastoma. *Nanoscale* **2020**, *12*, 23838–23850.

(56) Ali, M. M.; Liu, G.; Shah, T.; Flask, C. A.; and Pagel, M. D. Using two chemical exchange saturation transfer magnetic resonance imaging contrast agents for molecular imaging studies. *Acc. Chem. Res.* **2009**, *42*, 915–924.

(57) Kim, M.; Gillen, J.; Landman, B. A.; Zhou, J.; van Zijl, P. C. M. WAter Saturation Shift Referencing (WASSR) for chemical exchange saturation transfer experiments. *Magn. Reson. Med*. **2009**, *61*, 1441–1450.

Table of Contents Graphic